3870 Chem. Mater. **1998,** *10,* 3870−3878

Scanning Probe Microscopy Study of the Metal-Rich Layered Chalcogenides TaM_2Te_2 (M = Co, Ni)

Jörg Neuhausen,[†] Vladimir K. Evstaf'iev,[†] Thomas Block,[†] E. Wolfgang Finckh,[†]
Wolfgang Tremel,*,[†] Ludger Augustin,[‡] Harald Fuchs,[‡] Dirk Voss,[§]
Peter Krüger,[§] Albert Mazur,[§] and Johannes Pollmann[§]

Institut für Anorganische Chemie und Analytische Chemie der Johannes Gutenberg-Universität, Becherweg 24, D-55099 Mainz, Germany, Physikalisches Institut der Westfälischen Wilhelms-Universität Münster, Wilhelm Klemm-Strasse 10, D-48149 Münster, Germany, and Institut für Theoretische Physik II-Festkörperphysik der Westfälischen Wilhelms-Universität Münster, Wilhelm Klemm-Strasse 10, D-48149 Münster, Germany

Received April 21, 1998. Revised Manuscript Received September 11, 1998

The compounds $TaNi_2Te_2$ and $TaCo_2Te_2$ have been examined by scanning tunneling and atomic force microscopy. The title phases crystallize in layered structures with metal slabs sandwiched by tellurium atoms. Scanning probe microscope images of the surfaces of these materials arise from the surface tellurium atoms and—depending on the experimental conditions—can show very different features. The images have been simulated through surface charge densities calculated within the Extended Hückel and LMTO frameworks.

Introduction

In the past few years, the chemistry of transition metal tellurides has been extended to include metal-rich systems exemplified by the title phases $TaNi_2Te_2$ and $TaCo_2Te_2$, which adopt low-dimensional, i.e., layer type, structures.[1,2] These structures demonstrate the important bonding principle that early, electron-deficient transition metals (Nb, Ta) can interact strongly with electron-rich, late transition metals (Fe, Co, Ni), illustrating an unusual example of the Lewis base−Lewis acid interaction.[3] In the title compounds, CDW type interactions remain important: $TaCo_2Te_2$ has a structure type that can be described as the Peierls distorted version of $TaNi_2Te_2$.

Layered metal chalcogenides are almost ideally suited for investigations with surface scanning techniques such as scanning tunneling microscopy (STM) and atomic force microscopy (AFM). These scanning techniques are unique in that they can simultaneously probe the structural and electronic properties of surfaces with atomic resolution.[4,5] Besides surface imaging, the possibility of surface modification at an atomic scale has been demonstrated.[6] Many pioneering investigations have been performed on layered transition metal dichalcogenides such as TaS_2, or WSe_2.[7,8] The individual slabs of these phases contain sheets of metal atoms sandwiched between layers of chalcogen atoms. These layers stack to form three-dimensional arrangements. Since the individual layers are held together only by van der Waals interactions, these compounds are highly two-dimensional. Thus, crystals may be easily cleaved parallel to the layers and give clean and atomically flat surfaces. Therefore these materials are very attractive candidates for surface studies with scanning probe techniques.

Since the properties of these surfaces are of eminent importance for the cell performance in photovoltaic applications, their characterization by scanning probe techniques has been actively pursued.[9] Secondly, it has been found that surface deformations and modifications can be induced with the STM on a nanometer or even atomic scale at predefined positions without destroying the surface layer.[10,11] Finally, their polar surfaces make metal chalcogenides useful alternatives for the nonpolar graphite as substrates for the deposition of thin films.[12]

In this paper, we present experimental STM and AFM images of $TaNi_2Te_2$ and $TaCo_2Te_2$ obtained under different experimental conditions. These images are interpreted with the aid of the results of electronic structure calculations at both the extended Hückel and TB-LMTO-ASA level, using the standard interpretation that constant height STM images represent a small

---

[†] Johannes Gutenberg-Universität.

[‡] Physikalisches Institut der Westfälischen Wilhelms-Universität Münster.

[§] Institut für Theoretische Physik II-Festkörperphysik-der Westfälischen Wilhelms-Universität Münster.

(1) Tremel, W. *J. Chem. Soc. Chem. Commun.* **1991**, 1405.

(2) Tremel, W. *Angew. Chem.* **1992**, *104*, 230; *Angew. Chem., Int. Ed. Engl.* **1992**, *31*, 217.

(3) Brewer, L.; Wengert, P. *Metall. Trans.* **1973**, *4*, 83 and 2674.

(4) *Scanning Tunneling Microscopy*; Wiesendanger, R., Güntherod, H. J., Eds.; Springer-Verlag: Heidelberg, 1992.

(5) *Scanning Tunneling Microscopy and Spectroscopy*; Bonnell, D. A., Ed.; VCH Publishers: New York, 1993.

(6) Eigler, D. M.; Lutz, C. P.; Rudge, W. E. *Nature* **1991**, *352*, 600.

(7) Coleman, R. V.; Giambattista, B.; Hansma, P. K.; Johnson, A.; McNairy, W. W.; Slough, C. G. *Adv. Phys.* **1988**, *37*, 559.

(8) Wu, X. L.; Lieber, C. M. *Progr. Inorg. Chem.* **1991**, *39*, 431.

(9) Jiang, L.; Jaegermann, W.; Pettenkofer, C.; Tomm, Y.; Iyoda, T.; Hashimoto, K.; Fujishima, A. *Adv. Mater.* **1997**, *9* (7), 578.

(10) Fuchs, H.; Laschinski, R.; Schimmel, T. *Europhys. Lett.* **1990**, *13*, 307.

(11) Fuchs, H.; Schimmel, T. *Adv. Mater.* **1991**, *3*, 112.

(12) Fuchs, H.; Akari, S.; Dransfeld, K. *Z. Phys. B.* **1990**, *80*, 389.

10.1021/cm980714x CCC: $15.00

window near E_F of the local electron density $\rho(r_0,E_F)$ and that the AFM images represent the local electron density integrated over all states $\rho(r_0)$.

Experimental Section

Samples of $TaNi_2Te_2$ and $TaCo_2Te_2$ were synthesized from the elements as described in refs 1 and 2. The products were identified by X-ray powder diffraction. Large single crystals can be grown by chemical vapor-phase transport with halogens. The images shown in this article were obtained from crystals grown with iodine as transport agent, the temperatures of the cold and hot zone being 900 and 1000 °C, respectively.

Electronic Band Structure Calculations. *Extended Hückel Calculations.* Extended Hückel calculations within the tight-binding approximation[13−16] were performed for single layers of $TaNi_2Te_2$ and $TaCo_2Te_2$ with parameters given in the literature.[17,18] For surface charge density calculations a custom-made program was used.[19] Since the calculated charge densities at tip to surface distances (r_0) normally used in STM experiments (e.g. 5 Å) are too small for meaningful comparisons, a tip to surface distance r_0 of 1 Å was used for charge density plots. Similar values produced good agreement with experimental results for a large number of compounds.[20] For visualization of STM images taken at different bias voltages, an appropriate energy window was set for the charge density calculations.

TB-LMTO-ASA Calculations. TB-LMTO-ASA calculations on $TaNi_2Te_2$ were performed using version 47 of the TB-LMTO program.[21−23] To simulate surface properties, the band structure of a 2-fold superstructure of $TaNi_2Te_2$ was calculated, where every third layer and fourth layer were omitted. This led to a reduction of symmetry resulting in a monoclinic cell with $a' = 2c$, $b' = b$, $c' = a$ and $\beta = 90°$ with respect to the original $TaNi_2Te_2$ cell. The space group for this structure is $P2_1/m$ (No. 11). All k-space integrations were performed employing the tetrahedron method using 24 irreducible k-points in the monoclinic Brillouin zone. The basis set consists of s, p, and d orbitals of Ta and Ni, and s and p orbitals of Te. The positions of the empty spheres were determinined automatically by employing a method described by Krier et al.[21] The overlap was checked to be less than 16% for two atomic spheres, 18% for an atomic and an empty sphere, and less than 20% for two empty spheres. A listing of the positions and radii of the atomic and empty spheres for the nickel compound is given in Table 3. Charge densities were calculated for all occupied states. For visualizing STM images measured at different bias voltages, an appropriate energy window was set for the charge density calculations.

Microscopy Measurements. *STM Measurements.* STM images were obtained under ambient conditions using a Nanoscope II scanning tunneling microscope (Digital Instruments Inc.). The examined crystals were attached to a metal plate using silver glue and their surface was cleaved immediately before measurement using Scotch tape. Tips were mechanically prepared from Pt/Ir wire ($d = 0.25$ mm).

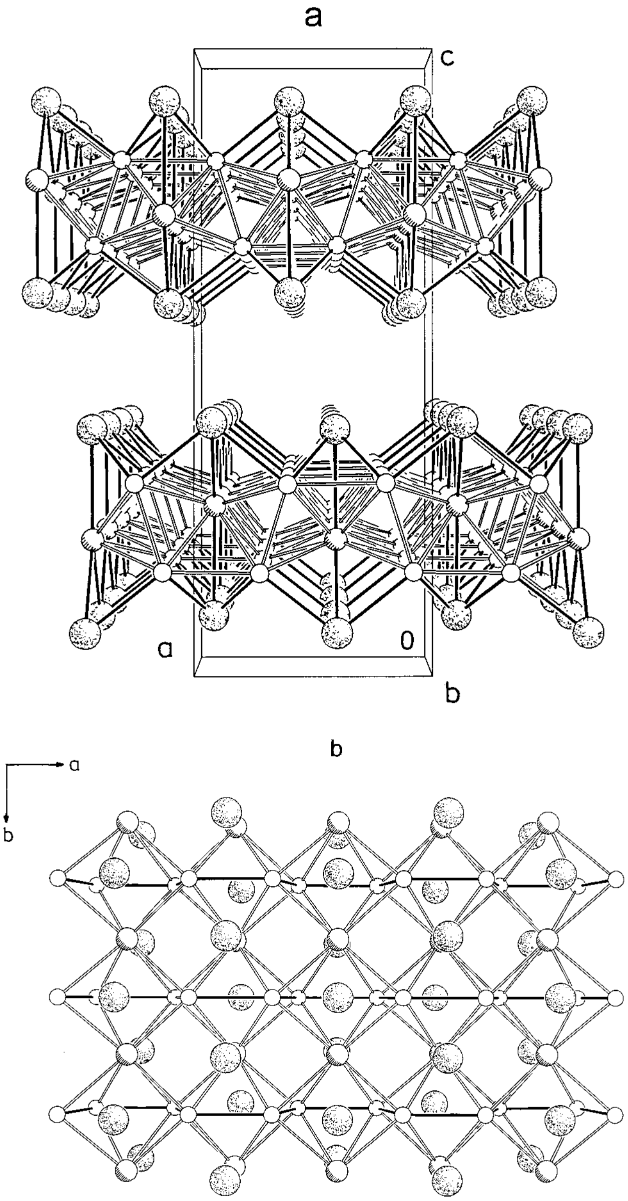

Figure 1. (a) Perspective view of the $TaNi_2Te_2$ structure along [010]; large dotted circles, Te; medium hatched circles, Ta; small open circles, Ni. (b) Projection of a single $TaNi_2Te_2$ layer along [001]; large dotted circles, Te; medium hatched circles, Ta; small open circles, Ni.

AFM Measurements. AFM measurements were perfomed under ambient conditions using an Explorer atomic force microscope (Topometrix GmbH) equipped with a 2.5 μm tube scanner. The crystals were mounted on the sample holder using double-sided Scotch tape and cleaved immediately before measurement. Commercial pyramidal shaped Si_3N_4 tips with a force constant of 0.064 N/m were used.

Results and Discussion

Crystal Structures. According to the results of single-crystal X-ray studies TaM_2Te_2 (M = Co, Ni)[1,2] crystallize in typical layer structures (Figure 1). A summary of crystallographic data is given in Tables 1 and 2. The metal atoms are sandwiched between Te layers. Van der Waals interactions prevail between the layers, the shortest Te−Te distance between the layers being approximately 3.7 Å. This is reflected in the fact that the crystals can be cleaved easily. The Te atoms

---

(13) Hoffmann, R. *J. Chem. Phys.* **1963**, *39*, 1397.

(14) Ammeter, J. H.; Bürgi, H.-B.; Thibeault, J. C.; Hofmann, R. *J. Am. Chem. Soc.* **1978**, *100*, 3686.

(15) Whangbo, M.-H.; Hoffmann, R. *J. Am. Chem. Soc.* **1978**, *100*, 6093.

(16) Whangbo, M.-H.; Hoffmann, R.; Woodward, R. B. *Proc. R. Soc. London, Ser. A* **1979**, *366*, 23.

(17) Calhorda, M. J.; Hoffmann, R. *Inorg. Chem.* **1988**, *27*, 3943.

(18) Canadell, E.; Mathey, Y.; Whangbo, M.-H. *J. Am. Chem. Soc.* **1988**, *110*, 104.

(19) Voss, D. Diploma Thesis, University of Münster, 1995.

(20) Magonov, S. N.; Whangbo, M.-H. *Surface Analysis with STM and AFM*; VCH: Weinheim, 1996 and references cited herein.

(21) Krier, G.; Jepsen, O.; Burkhardt, A.; Andersen, O. K. *Program TB-LMTO-ASA 47 (tight binding-linear muffin tin orbital-atomic sphere approximation)*, Stuttgart, 1996.

(22) Andersen, O. K. *Phys. Rev. B* **1975**, *12*, 3060.

(23) Andersen, O. K.; Jepsen, O. *Phys. Rev. Lett.* **1984**, *53*, 2571.

Table 1. Crystallographic Data for $TaNi_2Te_2$ and $TaCo_2Te_2$

formula	$TaNi_2Te_2$	$TaCo_2Te_2$
formula weight (g/mol)	553.5	554.0
crystal system	orthorhombic	orthorhombic
space group	$Pnma$ (No. 62)	$Pnma$ (No. 62)
lattice parameters (Å)	$a = 6.488(3)$ $b = 3.566(1)$ $c = 17.014(4)$	$a = 17.781(3)$ $b = 6.608(1)$ $c = 6.579(4)$
unit cell volume (Å^3)	393.6	773.0
formula units per cell	4	8
data collection at T (K)	298	298
crystal dimen (mm)	0.015 × 0.18 × 0.015	0.015 × 0.20 × 0.08
calcd density (g/cm^3)	9.339	9.520
diffractometer	Siemens R3	Siemens R3
radiation	Mo Kα ($\lambda = 0.71073$ Å)	Mo Kα ($\lambda = 0.71073$ Å)
linear absorption coefficient (1/mm)	51.29	51.02
monochromator	graphite, parallel	graphite, parallel
ang range measured	$4° \leq 2\theta \leq 80°$	$4° \leq 2\theta \leq 75°$
scan type	$\theta - 2\theta$	$\theta - 2\theta$
scan range	1.2° + Kα splitting	1.2° + Kα splitting
scan speed (deg/min)	variable, 1.8−14.6, depending on reflctn intensity	variable, 1.9−14.6, depending on reflctn intensity
octants measured	$+h, +k, \pm l$	$+h, +k, +l$
measured reflections	2231	2313
independent reflctns	1376	2115
R_{int}	0.028	0.011
obsd reflections ($F > 4\sigma(F)$)	1193	1659
absorption correction	semiempirical, Ψ-scan, ellipsoid	semiempirical, Ψ-scan, laminar
min. (max.) transmission	0.43 (0.94)	0.05 (0.43)
programs used	SHELXTL PLUS	SHELXTL PLUS
structure solution	direct methods	direct methods
structure refinement	full matrix least squares	full matrix least squares
minimized quantity	$\sum w(F_o - F_c)^2$	$\sum w(F_o - F_c)^2$
no. of parameters	32	53
weighting scheme	$w = 1/\sigma^2(F_o)$	$w = 1/\sigma^2(F_o)$
extinction correction[a]	0.0045	0.00033
$R(R_w)$[a]	0.038(0.033)	0.036(0.039)
goodness of fit (GOF)[c]	2.44	2.86
diff Fourier max. (e^-/Å^3)	4.9	4.8

[a] $F_c^{cor} = F_c(1 + 0.002\chi F_c^2/\sin(2\theta))^{-1/4}$. [b] $R = \sum||F_o| - |F_c||/\sum|F_o|$, $R_w = [\sum w||F_o| - |F_c||^2/\sum w|F_o|^2]^{1/2}$. [c] $GOF = [\sum w||F_o| - |F_c||^2/m - n]^{1/2}$, where m and n are the numbers of data and parameters, respectively.

Table 2. Positional Parameters and Equivalent Isotropic Thermal Parameters (U_{eq},[a] Å^2) for $TaNi_2Te_2$ and $TaCo_2Te_2$

atom	Wyckoff position	x/a	y/b	z/c	U_{eq}
		$TaNi_2Te_2$			
Ta	*4c*	0.90484(5)	1/4	0.27681(2)	0.0043(1)
Ni(1)	*4c*	0.6006(2)	3/4	0.31644(6)	0.0059(3)
Ni(2)	*4c*	0.7117(2)	3/4	0.18147(6)	0.0060(3)
Te(1)	*4c*	0.90874(9)	1/4	0.10469(3)	0.0065(1)
Te(2)	*4c*	0.90413(9)	3/4	0.40858(3)	0.0055(1)
		$TaCo_2Te_2$			
Ta(1)	*4c*	0.27815(3)	1/4	0.6505(1)	0.0065(1)
Ta(2)	*4c*	0.23485(3)	1/4	0.1513(1)	0.0056(1)
Co(1)	*8d*	0.18111(7)	0.0342(2)	0.8451(2)	0.0065(3)
Co(2)	*8d*	0.18091(7)	0.0329(2)	0.4564(2)	0.0073(3)
Te(1)	*4c*	0.39315(5)	1/4	0.1536(2)	0.0080(2)
Te(2)	*4c*	0.08670(5)	1/4	0.6496(2)	0.0074(2)
Te(3)	*8d*	0.40629(3)	−0.0030(1)	0.65072(9)	0.0078(2)

Table 3. Positional Parameters and Radii of Atomic and Empty Spheres Used for the Calculation of Charge Densities of $TaNi_2Te_2$[a]

sphere	x	y	z	R(Å)
Ta1	0.11160	0.25000	0.59516	1.75260022
Ta2	0.13840	0.25000	0.09516	1.75260978
Ni1	0.09178	0.75000	0.89940	1.34931596
Ni2	0.09074	0.75000	0.28830	1.34798117
Ni3	0.15926	0.75000	0.78830	1.34799473
Ni4	0.15822	0.75000	0.39940	1.34932524
Te1	0.05234	0.25000	0.09126	1.61419613
Te2	0.04571	0.75000	0.59587	1.57043514
Te3	0.20429	0.75000	0.09587	1.57042156
Te4	0.19766	0.25000	0.59126	1.61418256
E1	0.00000	0.75000	0.22673	2.13112424
E2	0.26619	0.75000	0.51107	2.13640951
E3	0.29514	0.75000	0.01383	2.13640951
E4	0.34749	0.25000	0.62495	2.13640951
E5	0.39996	0.75000	0.01383	1.90386560
E6	0.42274	0.75000	0.49647	1.72863994
E7	0.45215	0.25000	0.24935	1.53054550
E8	0.47952	0.25000	0.78467	1.38438885

[a] The cell is monoclinic, space group $P2_1/m$ (No. 11). The lattice constants are $a' = 2c$, $b' = b$, $c' = a$, and $\beta = 90°$ with respect to the original (orthorhombic) $TaNi_2Te_2$ cell.

of the top and bottom sheet form a close-packed arrangement (Figure 2). These close-packed surfaces can be imaged using scanning probe techniques. Here it is important to notice that both $TaNi_2Te_2$ and $TaCo_2Te_2$ have crystallographically nonequivalent Te atoms that differ in height with respect to the surface and thus give rise to charge density maxima of different height and shape in the SPM images. In $TaNi_2Te_2$ there are two of these atoms, Te(1) and Te(2), forming alternating rows running parallel to b, Te(2) being higher by 0.23 Å than Te(1) (Figure 2a). The $TaCo_2Te_2$ structure, which represents a distorted variant of $TaNi_2Te_2$,[2] contains three nonequivalent Te atoms. Again these atoms form alternating rows running parallel to b. As illustrated in Figure 2b, one row is formed by the Te(1) and Te(2) atoms, while the second row consists of the Te(3) atoms. Te(1) and Te(2) are located 0.23 Å lower and 0.12 Å higher than the Te(3) atoms, respectively.

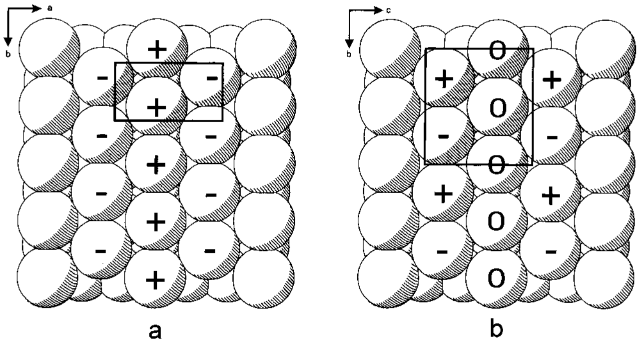

Figure 2. (a) Space-filling representation of a $TaNi_2Te_2$ layer. The Te(1) and Te(2) atoms forming rows parallel to *b* located 0.23 Å lower and higher with respect to the surface, respectively, are indicated by (−) and (+). The unit cell is indicated by a rectangle. (b) Space-filling representation of a $TaCo_2Te_2$ layer. The Te(1) and Te(2) atoms located 0.23 Å lower and 0.12 Å higher with respect to the Te(3) atoms, respectively, are indicated by (−) and (+). The Te(3) atoms are labeled (0). The unit cell is indicated by a rectangle.

STM and AFM Imaging. For scanning tunneling microscopy (STM) images, a tunneling current between a metallic tip and the surface is measured, while the tip is scanning the surface. Depending on the bias voltage between tip and sample, electrons can tunnel from the tip into unoccupied surface states right above the Fermi level ($U_{\text{bias}} > 0$) or from occupied surface states just below the Fermi level to the tip ($U_{\text{bias}} < 0$). Thus, provided that tip−surface interactions are negligible, an STM image represents the partial density of states of the sample surface at the Fermi level $\rho(r_0,E_F)$ at the tip to sample distance r_0.[24,25] For different bias voltages, electrons from the corresponding energy windows ranging from E_F to $E_F + eU_{\text{bias}}$ can be involved in the tunneling process.

In contact mode atomic force microscopy (AFM), the repulsive force introduced primarily by the overlap of the electron densities between a sharp tip and the sample is measured while the tip is scanning the sample surface. Neglecting tip−sample interactions and approximating the tip as a single atom, the repulsive force between tip and sample is proportional to the local density of states of the sample at the tip position summed up over all occupied band levels.[18] Therefore, constant height AFM images can be correlated with the total electron density of the sample surface at the tip to sample distance, $\rho(r_0)$.

Recently, a large number of scanning probe microscopy (SPM), i.e., STM and AFM, images of layer type materials have been interpreted using the results of surface charge density calculations at the extended Hückel (EH) level.[18,26−30] Since this method has some limitations due to its semiempirical character, we have employed the LMTO method for calculation of surface charge densities for $TaNi_2Te_2$. In the following, we compare the results of both EH and LMTO surface charge density calculations. Furthermore, an interpretation of the experimental STM and AFM images is given based on the computational results.

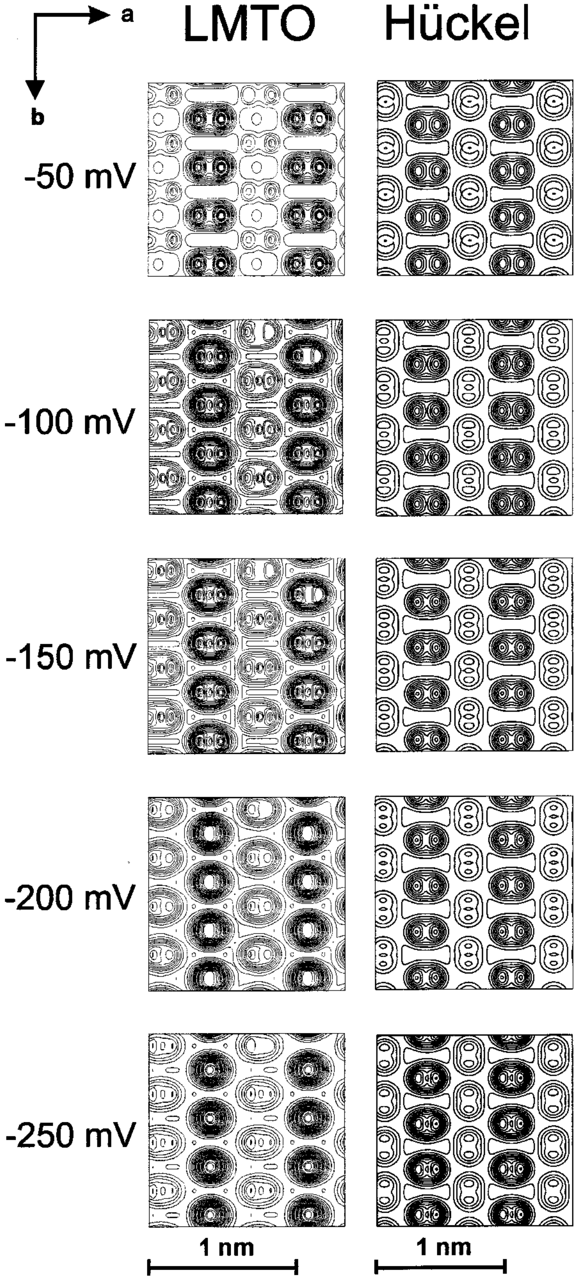

Figure 3. Comparison of surface charge density plots obtained for different energy windows using the LMTO and EH methods. The Te(2) atoms give rise to rows of charge density maxima with dense contour lines parallel to *b*, whereas the charge density of the Te(1) atoms shows maxima with lower density of contour lines.

A comparison between the results of EH and LMTO surface charge density calculations on $TaNi_2Te_2$ for several different bias voltages is given in Figure 3. All calculated patterns show a pseudohexagonal arrangement of charge density maxima, which can be related to the positions of the surface Te atoms. This shows, that despite the dominance of metal centered states around the Fermi level, the surface charge density near the Fermi level originates primarily from the surface atoms, i.e., tellurium, as was shown for other metal

---

(24) Tersoff, J.; Hamman, D. R. *Phys. Rev. B* **1985**, *31*, 805.
(25) Tersoff, J. *Phys. Rev. Lett.* **1986**, *37*, 440.
(26) Magonov, S. N.; Whangbo, M.-H. *Adv. Mater.* **1994**, *6*, 355.
(27) Bengel, H.; Cantow, H.-J.; Magonov, S. N.; Monconduit, L.; Evain, M.; Liang, W.; Whangbo, M.-H. *Adv. Mater.* **1994**, *6*, 649.
(28) Whangbo, M.-H.; Ren. J.; Canadell, E.; Louder, D.; Parkinson, B. A.; Bengel, H.; Magonov, S. N. *J. Am. Chem. Soc.* **1993**, *115*, 3760.
(29) Magonov, S. N.; Zönnchen, P.; Rotter, H.; Cantow, H.-J.; Thiele, G.; Ren. J.; Whangbo, M.-H. *J. Am. Chem. Soc.* **1993**, *115*, 2495.
(30) Kim, S.-J.; Park, S.-J.; Jeon, I. C.; Kim, C.; Pyun, C.; Yee, K. A. *J. Phys. Chem. Solids* **1997**, *58*, 659.

chalcogenide systems.[18,26-28,30] This is not surprising considering the exponential decrease of wave functions with increasing distance.

The charge density maxima can be divided into alternating rows of different electron density, which run parallel to the crystallographic *b* axis. The rows correspond to the two crystallographically nonequivalent Te atoms. The row of charge density maxima with higher electron density is generated by the Te(2) atoms, which are located closer to the tip by 0.23 Å, while the row of charge density maxima with a lower electron density corresponds to the Te(1) atoms. The bias voltage dependence of the electron densities obtained from the two computational methods differ in some details. As one moves from more negative to less negative bias voltages, the electron density distribution above Te(2) gradually splits along the crystallographic *a* axis in the LMTO results. The electron density peak corresponding to Te(2) changes from being nearly spherical at $U_{\mathrm{bias}} = -250$ mV to a bilobal shape at $U_{\mathrm{bias}} = -50$ mV. This splitting is noticeable at $U_{\mathrm{bias}} = -150$ mV and less negative bias voltages. On the other hand, the results of EH calculations show a bilobal shape of the Te(2) electron density for all bias voltages shown in Figure 3. The degree of splitting depends on the bias voltage in a way similar to the LMTO results. As one moves from less negative to more negative values of U_{bias}, the splitting decreases. In fact, for a bias voltage of -400 mV the EH method yields a spherical electron density distribution as well.

Looking at the row of charge density maxima with lower electron density corresponding to the Te(1) atoms, one observes a bilobal electron density distribution for all calculations. However, the orientation of the bilobal charge density maxima is different in the LMTO results compared to the EH calculation. Whereas in the charge density plot obtained from LMTO the Te(1) bilobes are oriented parallel to the *a* axis, the EH results yield bilobes with the long axis along the *b* direction.

Figure 4a shows an experimental STM image of $TaNi_2Te_2$ taken at a bias voltage of $U_{\mathrm{bias}} = -200$ mV and a tunneling current of $I_t = 1$ nA. The pseudohexagonal arrangement of the single atoms is clearly visible. The lattice constants obtained by X-ray diffraction are reproduced fairly well. One can clearly distinguish two rows of different brightness, which can be associated with the two crystallographically nonequivalent Te atoms. The shape of the charge density maxima in the experimental image is nearly spherical. All these observations are reproduced very well in the charge density plot derived from LMTO band calculations for the given energy window ranging from E_F to $E_F - 0.2$ eV, which is shown in Figure 4b. Parts c and d of Figure 4 show an experimental STM image of $TaNi_2Te_2$ taken at $U_{\mathrm{bias}} = -50$ mV and $I_t = 1$ nA as well as the corresponding charge density plot obtained from LMTO calculations. As pointed out above, switching the bias voltage to -50 mV results in a splitting of the electron densities for the charge density maxima of the brighter Te(2) row to a bilobal shape in the calculated charge density. This feature is reproduced well in the experimental image, which shows bright rows of charge density maxima with a bilobal shape that can be associated with the Te(2) atoms. Between these rows no bright charge density maxima are observed, in accordance with the larger difference in electron density between Te(2) and Te(1) calculated for this energy window. While there is a mirror plane perpendicular to the *b*-axis in the calculated electron density, this symmetry element cannot be observed in the experimental image. This deviation may be attributed to image distortions due to drift of the piezo element.

An experimental AFM image of $TaNi_2Te_2$ is shown in Figure 5 together with the corresponding calculated total surface charge density. The pseudohexagonal arrangement of the surface atoms is reproduced in both images. The calculated charge density plot consists of alternating rows of spherically shaped charge density maxima running along *b*, where—in contrast to geometrical considerations—the rows of higher charge density maxima arise from the less elevated Te(1) atoms. This clearly shows the importance of surface charge density calculations for the interpretation of SPM images. The spherical shape of charge density maxima is expected, since the *total* charge density around an atom—including all electronic states should be approximately spherical. All these features are found in the experimental image as well, where one can observe alternating bright and less bright rows of spherically shaped spots.

Charge density calculations for $TaCo_2Te_2$ could only be performed using the EH method for technical reasons. The problem is too large for treatment with the standard LMTO package. The calculated charge density patterns for $TaCo_2Te_2$ are slightly more complex compared to $TaNi_2Te_2$ due to the fact that there are three crystallographically nonequivalent Te atoms with different heights with respect to the surface.

A plot of the calculated total electron density is shown in Figure 6a. Again, the charge density plot shows a pseudohexagonal symmetry, and the charge density maxima can be divided into two different rows running parallel to the *b*-axis. One row is formed by the Te(1) and Te(2) atoms, which are located 0.23 Å lower and 0.12 Å higher than the Te(3) atom, respectively, while the second row is formed by the Te(3) atoms. Thus, from geometrical considerations one would expect a charge density pattern with two alternating rows running parallel to *b*, one row of equal charge density maxima with intermediate charge density, and a second row with alternating charge density maxima of lower and higher densities. This is confirmed by the computational results (Figure 6a). In the experimental AFM image depicted in Figure 6b, one can observe the pseudohexagonal arrangement of charge density maxima. The lattice constants obtained from crystallography are reproduced well. However, it is not possible to distinguish charge density maxima with different height as expected for the three nonequivalent Te atoms in the experiment. This effect may arise from tip imperfections. Height resolution is lost if the tip shape deviates from the ideal (i.e. single atom) geometry.

The charge densities calculated for $TaCo_2Te_2$ show a very complex dependence on the energy window chosen. Figure 7a shows the calculated charge density of the $TaCo_2Te_2$ surface within the energy window ranging from E_F to $E_F + 0.1$ eV. The calculated charge density distribution resembles the structure of the surface Te

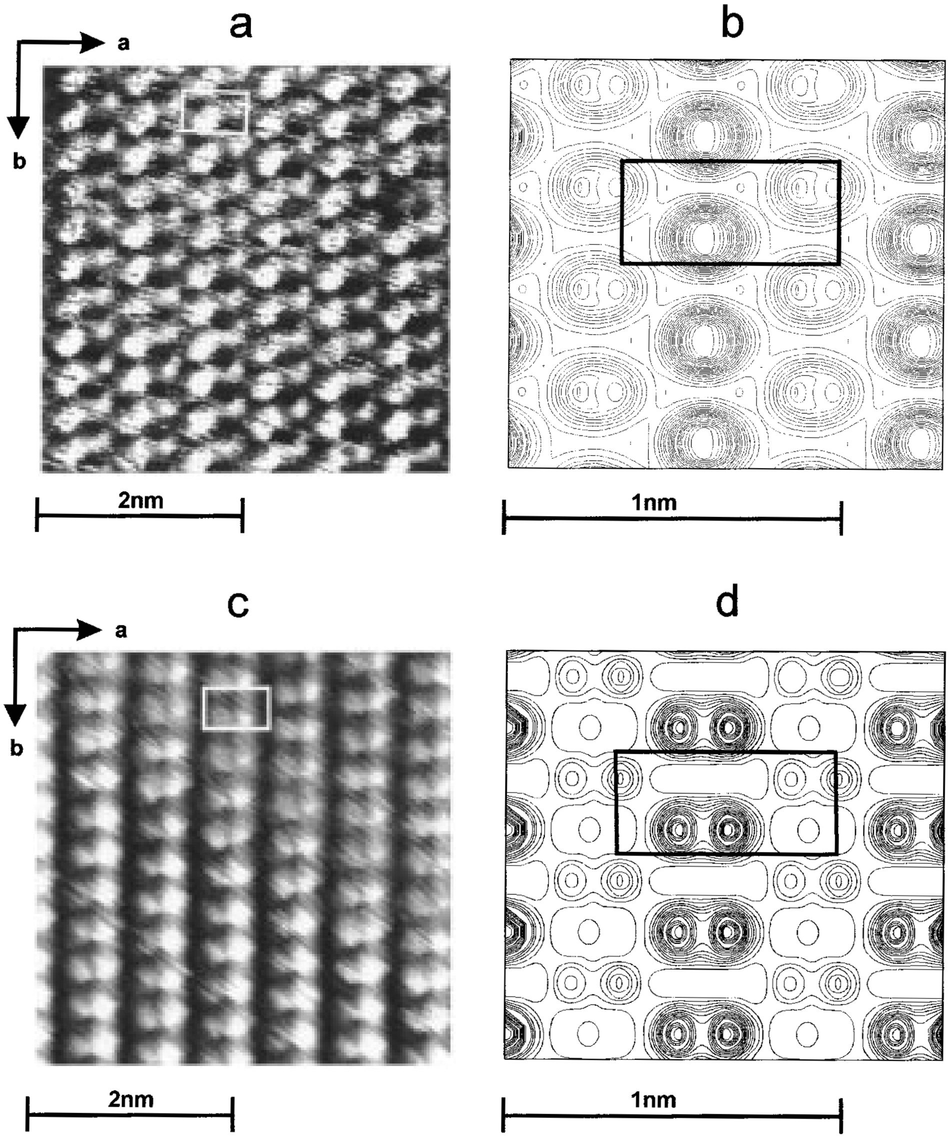

Figure 4. Comparison of experimental STM images of a $TaNi_2Te_2$ surface obtained at different bias voltages and the corresponding calculated (LMTO) surface charge densities. (a) experimental STM image taken at $U_{\text{bias}} = -200$ mV and $I_t = 1$ nA. (b) surface charge density calculated using an energy window ranging from E_F to $E_F - 0.2$ eV. (c) experimental STM image taken at $U_{\text{bias}} = -50$ mV and $I_t = 1$ nA. (d) surface charge density calculated using an energy window ranging from E_F to $E_F - 0.05$ eV. The Te(2) atoms give rise to rows of charge density maxima with dense contour lines parallel to *b*, whereas the charge density of the Te(1) atoms shows maxima with lower density of contour lines.

atoms obtained from crystallography. Three different Te atoms can be distinguished in the calculated charge density. The electron density distribution above the Te(3) atoms is distorted from spherical symmetry in a way that the maximum of the electron density is shifted from the center of the sphere in the *y*-direction in an alternating fashion, thus giving rise to a doubling of the *b*-axis compared to $TaNi_2Te_2$. The charge density maxima corresponding to Te(2) are elongated in the *b*-direction and show some splitting. The charge density maxima originating from Te(1) on the other hand are slightly elongated in the *c*-direction. The heights of the charge density maxima in the calculated diagram do not resemble the geometrical features of the structure. Considering the height of the different Te atoms, one would expect the intensities of the charge density maxima corresponding to the three Te atoms to decrease in the order Te(2) > Te (3) > Te(1), whereas the calculated charge densities for the three atoms are similar. This clearly shows the influence of the energy window—and hence the electronic states within this window—on the STM images. This again shows the importance of charge density calculations for the interpretation of SPM images. The charge density distribution of the calculated image is well reproduced in the experiment. An image taken at $U_{\text{bias}} = 100$ mV and $I_t = 1.0$ nA (Figure 7b) shows a nearly hexagonal arrangement of charge density maxima with nearly equal height. The distances of the charge density maxima agree well with the crystallographic results, although some distortion from orthorhombic symmetry is observed due to piezo drift. The deviation of the charge density from spherical symmetry cannot be resolved in the experimental image. Also, the doubling of the unit cell is not observed in the experimental image. These deviations between observed and calculated images may be attributed to tip imperfections or adsorption processes under ambient conditions.

A plot of the calculated charge density of a $TaCo_2Te_2$ surface within the energy window ranging from E_F to

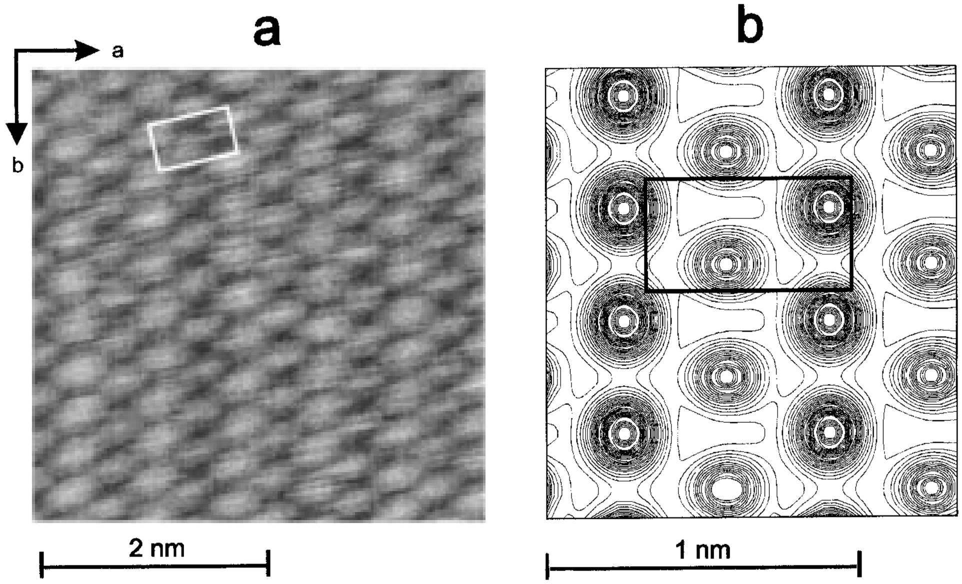

Figure 5. (a) Experimental AFM image of a $TaNi_2Te_2$ surface and (b) total surface charge density calculated using the LMTO method. Here, the Te(1) atoms give rise to rows of charge density maxima with dense contour lines parallel to *b*, whereas the charge density of the Te(2) atoms shows maxima with lower density of contour lines.

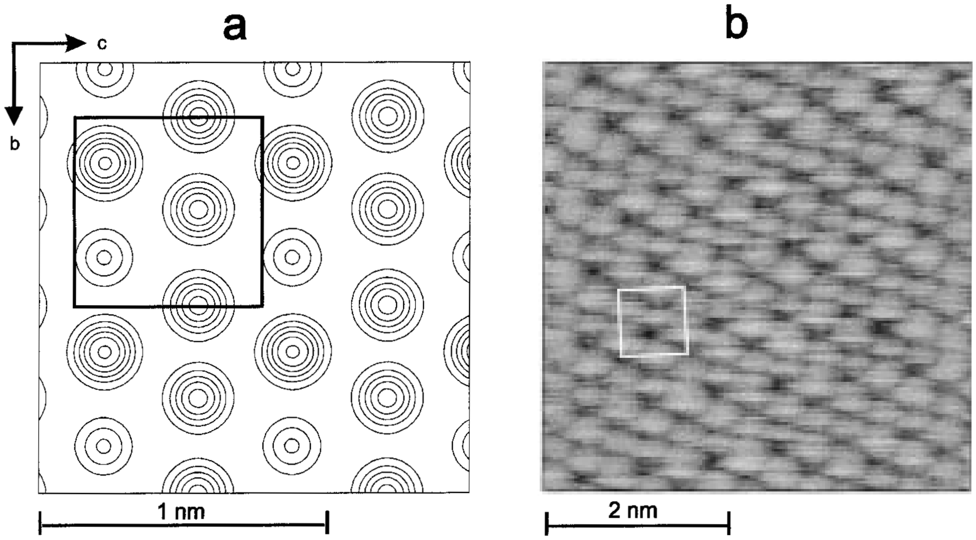

Figure 6. (a) Total surface charge density of $TaCo_2Te_2$ calculated using the EH method and (b) experimental AFM image of a $TaCo_2Te_2$ surface. The rows of charge density maxima with uniform height parallel to *b* are formed by the Te(3) atoms, whereas the rows with alternating higher and lower charge density result from the Te(2) and Te(1) atoms, respectively.

$E_F - 0.1$ eV is given in Figure 7c, together with the corresponding experimental STM image taken at $U_{bias} = -100$ mV and $I_t = 2.4$ nA (Figure 7d). Again, the calculated charge density distribution resembles the structure of the surface Te atoms obtained from crystallography. The charge distribution around the three different Te atoms shows deviations from spherical symmetry, very similar to the results obtained for the energy window E_F to $E_F + 0.1$ eV displayed in Figure 7a. However, the charge densities calculated for the different atoms for the interval E_F to $E_F - 0.1$ eV decrease in the order Te(3) > Te(2) > Te(1). Thus, the charge density distribution differs clearly from that obtained for the energy window E_F to $E_F + 0.1$ eV. On the basis of the computational results, the experimental image (Figure 7d) may be interpreted in the following way: The bright charge density maxima can be attributed to the Te(3) atoms, which form an approximately square-shaped lattice with a repeat of ~7 Å, in good agreement with the lattice constants *b* and *c* obtained from the crystallographic studies. Moving along the *b*-direction, one observes two Te(3) atoms per lattice repeat, whereas the Te(3)−Te(3) distance in *c*-direction corresponds to a full lattice repeat. Moving along *b*, one observes rows of Te(3) atoms with alternating intensities, whereas rows of charge density maxima with equal intensities, but shifted parallel to *b* in an alternating fashion, would be expected from the computational results. These differences may be attributed to tip−sample interactions. The less bright charge density maxima located inside the rectangles formed by four neighboring Te(3) atoms may be assigned to the Te(2) atoms, which should give rise to the second brightest charge density maxima according to the results of the charge density calculations. For these charge density maxima, a shift from the crystallographically determined position is observed in the experimental STM image, which may again arise from

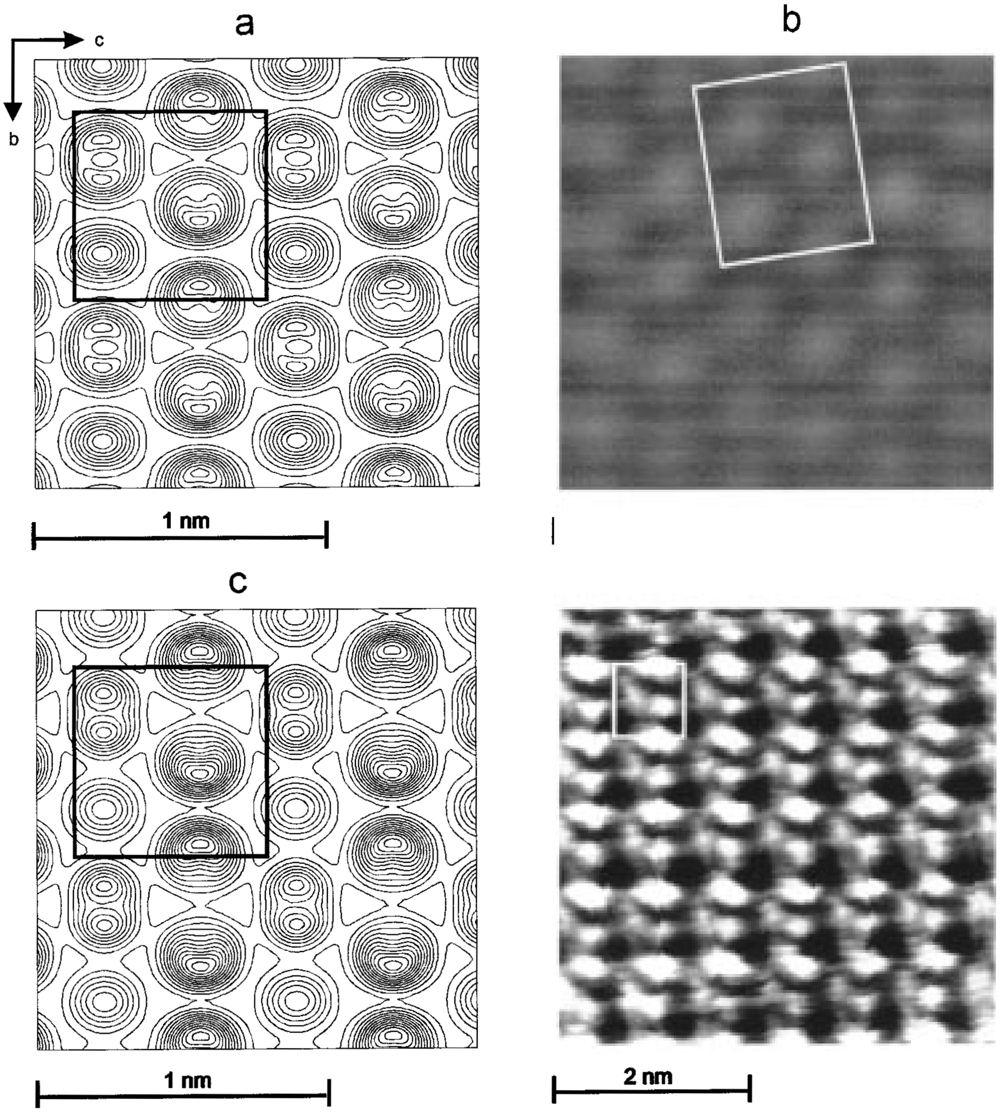

Figure 7. (a) Surface charge density of TaCo$_2$Te$_2$ calculated using the EH method for an energy window ranging from E_F to E_F + 0.1 eV and (b) experimental STM image of a TaCo$_2$Te$_2$ surface taken at U_{bias} = 100 mV and I_t = 1.0 nA (Fourier filtered). (c) surface charge density of TaCo$_2$Te$_2$ calculated using the EH method for an energy window ranging from E_F to E_F − 0.1 eV and (d) experimental STM image of a TaCo$_2$Te$_2$ surface taken at U_{bias} = −100 mV and I_t = 2.4 nA. The rows of charge density maxima parallel to *b* with distorted spherical symmetry are formed by the Te(3) atoms, whereas the rows with alternating bilobal and spherical charge density distribution result from the Te(2) and Te(1) atoms, respectively.

tip−sample interactions. Finally, there is no feature in the experimental image which can be assigned to the Te(1) atoms, for which the calculated charge density is by far lowest. Hence, the theoretically determined density distribution and the experimental STM image agree fairly well. Again, we observe a violation of the crystallographic symmetry in the experimental image. A mirror plane perpendicular to the *b*-axis is missing. As in the case described above (Figure 4c,d), this could be caused by drifts of the piezo element.

Conclusion

Crystal surfaces of the layered tellurides TaNi$_2$Te$_2$ and TaCo$_2$Te$_2$ have been investigated by AFM and STM measurements. The obtained images can be rationalized using the results of electronic structure calculations of different levels of accuracy. The results of charge density calculations prove to be very helpful in assigning the different features of the SPM images to the different surface atoms. Furthermore, the results of charge density calculations using the tight binding extended Hückel and LMTO methods are compared.

AFM and STM images of TaNi$_2$Te$_2$ and TaCo$_2$Te$_2$ are interpreted with the aid of plots of the calculated total surface charge density (AFM) and surface charge density close to the Fermi level (STM). The calculated charge densities obtained using the EH and the LMTO approach are very similar concerning the absolute values of charge density, whereas there are some small differences in the shape of the density distributions obtained by the two methods. The calculated charge density peaks and the charge density maxima in the STM and AFM images can be associated with the surface tellurium atoms. The arrangement of the charge density maxima resemble the surface structure expected from X-ray diffraction investigations.

For TaNi$_2$Te$_2$, the experimental STM images very closely resemble the corresponding calculated charge density plots concerning both the height and the shape of the charge density maxima. One can observe alternating rows of higher and lower charge density maxima which change the shapes as well as intensities as one lowers the bias voltage.

The experimental AFM image of $TaNi_2Te_2$ is in good agreement with the calculated total surface charge density as well. Both show a pattern of alternating bright and less bright rows which can be associated with surface tellurium atoms. In contrast to geometrical considerations, the higher charge density maxima are associated with the lower lying Te atoms, whereas the charge density around the more elevated Te atoms, which are located closer to the tip, is lower.

The AFM images of $TaCo_2Te_2$ agree with the calculated charge density pattern as far as they show a pseudohexagonal arrangement of surface atoms, which was expected considering the results of structure determination. The calculated charge density plot shows different heights of the charge density maxima associated with the three nonequivalent surface tellurium atoms. This feature could not be confirmed in the experimental images obtained so far. This effect is likely to be the result of tip imperfections.

The experimental STM images of $TaCo_2Te_2$ compare well with the calculated electron density patterns concerning the relative intensities of the charge density maxima assigned to the different Te atoms. Here, the results of charge density calculations proved essential for assigning charge density maxima to the crystallographically nonequivalent surface Te atoms, which have a different height with respsect to the tip. The height of the charge density maxima are strongly affected by the bias voltage and hence on the electronic states involved in the tunneling process. Some deviations between calculated and experimental images are observed as well as a distortion of the experimental images. This may be attributed to tip imperfections, sample contamination, and piezo drift.

Acknowledgment. Financial support from the Bundesministerium für Forschung und Technologie under the contract number DLR-2A523370-03N1023C1 is gratefully acknowledged. The LMTO program package was kindly supplied by Prof. O. K. Andersen (Stuttgart). The Mainz group thanks Dr. O. Jepsen and Dr. C. Felser for help with the programs. We are indebted to Dr. J. Peters (H.C. Starck, Goslar) for a donation of Nb and Ta powder, Dr. G. Höfer (Heraeus Quarzschmelze, Hanau) for generous gifts of silica tubes, and the Fonds der Chemischen Industrie for financial support. Dr. Ram Seshadri is thanked for many helpful discussions.

CM980714X